International Journal of Thermal Sciences 139 (2019) 176–185

Contents lists available at ScienceDirect

International Journal of Thermal Sciences

journal homepage: www.elsevier.com/locate/ijts

Numerical and experimental study of heat-transfer characteristics of needle-to-ring-type ionic wind generator for heated-plate cooling

S. Wang, J.G. Qu, L.J. Kong, J.F. Zhang*, Z.G. Qu

Key Laboratory of Thermo-Fluid Science and Engineering, Ministry of Education, School of Energy and Power Engineering, Xi'an Jiaotong University, Xi'an, 710049, China

ARTICLE INFO

Keywords:
Ionic wind
Needle-to-ring
Numerical simulation
Experiment
Cooling
Hot spot

ABSTRACT

Ionic wind generators have shown significant application potential in devices for cooling, air actuation, and flow control. In this study, a needle-to-ring electrode ionic wind generator with optimized parameters was employed to cool a heated copper plate. A three-dimensional numerical simulation was conducted to obtain the electric, flow, and temperature fields of the ionic wind generator. To verify the ionic wind generator's capacity to cool the heated plate, an ionic wind generator prototype was fabricated and experimentally tested. The temperature distribution of the plate heated by a uniform distributed heat flux and non-uniform heat flux with a local hot spot was analyzed. Results show that the applied voltage should be less than the threshold voltage of spark discharge to ensure effective and stable operation of the ionic wind generator. When the plate is heated by a uniform heat flux, the temperature distribution in most areas around the center of the plate is relatively uniform. If a hot spot exists, the temperature of the central plate is higher than that of the surrounding areas, and the radial temperature difference gradually increases with the increase of the hot-spot heat flux. Moreover, the high-temperature area in the center of the plate gradually expands with increasing hot-spot radius. Besides, the increase in the copper plate thickness has little influence on the final temperature distribution. The heated plate with a uniform heat flux below 2 kW/m^2 could be cooled to below 80 °C by the ionic wind generator at an applied voltage of 11 kV. When the plate is heated by a non-uniform heat flux with a hot spot, compared with the experimental results of natural convection, ionic wind can effectively reduce the temperature of the plate (a temperature drop of at least 45 °C was observed). This study provides a potential solution for commercial chip cooling with needle-to-ring-type ionic wind generators.

1. Introduction

Ionic wind is the air flow driven by an electric discharge field. When a high voltage is applied between electrodes, air molecules around the corona electrode are ionized under an uneven electric field. The ionized air molecules are accelerated by Coulomb force and then collide with neutral air molecules, thereby resulting in momentum transfer to the neutral molecules. Thus, an air stream is formed between the corona and collector electrodes. Fig. 1 shows the basic principles of ionic wind generation. Wind-driven devices based on the ionic wind principle have shown significant potential in fields such as electronic cooling [1,2], flow control [3,4], and air actuation [5,6] because of advantages such as low energy consumption, absence of moving parts, compact structure, and flexible design. Numerous electrode geometries have been proposed for ionic wind generators, including wire-to-plate [7], wire-to-cylinder [8], needle-to-plate [9], and needle-to-grid [10].

In the past few years, many studies have explored the enhancement of natural and forced convection heat transfer using ionic wind generators with various configurations. Owsenek and Seyyed-Yagoobi [11] experimentally investigated the electro-hydrodynamic (EHD) enhancement of natural convection using an ionic wind device with a needle-to-plate structure. Go et al. [12]discussed the local cooling enhancement of bulk flow due to ionic winds, and a more than two-fold enhancement of local heat-transfer coefficient was observed. Heat-transfer enhancement for a plate-fin heat sink subject to needle-arrayed electrodes was experimentally investigated by Huang et al. [13]; the enhancement ratio was 3–5 with a preferable electrode height. Pour and Esmaeilzadeh [14] experimentally investigated the heat-transfer enhancement of a cylindrical heat source using an EHD actuator in a duct. It was found that the heat-transfer enhancement is more effective at a low Reynolds number.

Among the various types of configurations, a needle-to-ring type is of particular interest because of the high permeability of the collector electrode, the flexible modification of the ring electrode, and the

* Corresponding author.
E-mail address: zhangjf@mail.xjtu.edu.cn (J.F. Zhang).

https://doi.org/10.1016/j.ijthermalsci.2019.01.032
Received 28 November 2017; Received in revised form 13 December 2018; Accepted 24 January 2019

Nomenclature

c	Specific heat, $J{\cdot}kg^{-1}K^{-1}$
d	Diameter of needle electrode, mm
D	Diameter of ring electrode, mm
E	Electric field intensity, $V{\cdot}m^{-1}$
F	Electric force, N
G	Gaps between two electrodes, mm
h	Heat transfer coefficient, $W{\cdot}m^{-2}K^{-1}$
I	Current, A
J	Current density, $A{\cdot}m^{-2}$
l	Length of needle electrode, mm
T	Temperature, K
P	Power, W
p	Pressure, Pa
q	Space-charge density, $C{\cdot}m^{-3}$ /(heat flux), $W{\cdot}m^{-2}$
r	Distance from plate center
x	Gap between outlet and plate surface
Q_e	Joule heat, J
R	Radius of ring electrode, mm
U	Velocity, m/s
V	Voltage, V
W	Length of square plate

Greek Symbols

μ_E	Ionic mobility, $m^2{\cdot}V^{-1}s^{-1}$
ν	Kinematic viscosity, $m^2{\cdot}s^{-1}$
ρ	Density, kgm^{-3}
δ	Experimental error

Subscripts

0	Initial value or standard value
a	ambient value
e	Value under electric field
f	Value of heat flux
h	Value of hot spot
max	Value of maximum

potential for application of generators in a row or series. The flow speed in a wind generator with a needle-to-ring configuration is approximately 1–5 m/s according to experimental results [15,16]. Considerable efforts have been devoted to designing the electrode configurations that are effective for achieving high-speed airflow. For example, Rickard and Dunn-Rankin [17] measured the dependence of the ionic wind velocity on the distance between electrodes for specific diameters and lengths of collector electrodes. Moreau et al. [18] reported that the serial connection of multiple needle-to-cylinder ionic wind generators can increase the airflow velocity. Kawamoto et al. [19] used a needle-plate-type ionic wind generator to study the ionic wind flow, heat-transfer enhancement, and rules of ozone generation. In Kawamoto's work, the collector electrode is a plate with a hole in the center. Qiu et al. [20] proposed a needle-array–to–ring-type serial-staged EHD gas pump under negative corona discharge. In their study, the flow velocity was dependent on the stage number and pressure loss, and a maximum velocity of 7.39 m/s was achieved. Lee [21] reported an integrated needle-to-ring-type ionic wind generator and enhanced the volumetric flow rate on the basis of a large cross-sectional area. The interference between parallel air jets was reduced by adding a shielding layer between two electrode boards. Li et al. [22] suggested an empirical model for the ionic wind velocity as a function of the geometric factors.

Most of the aforementioned studies are based on experiments, while numerical methods can provide further details about the velocity and temperature field at a lower cost. Furthermore, few studies have focused on the heat-transfer performance of generators with needle-to-ring electrodes for cooling a heated plate with uniform flux and non-uniform heat flux, while the impinging flow of the generators has the potential for local cooling of microelectronics.

In the work reported in this paper, an optimized ionic wind generator with a needle-to-ring electrode system was fabricated and experimentally studied to analyze its cooling capacity for a heated plate with a uniform heat flux and non-uniform heat flux with a local hot spot. The influences of the applied voltage, heat flux, and hot spot on the cooling capacity are discussed in detail.

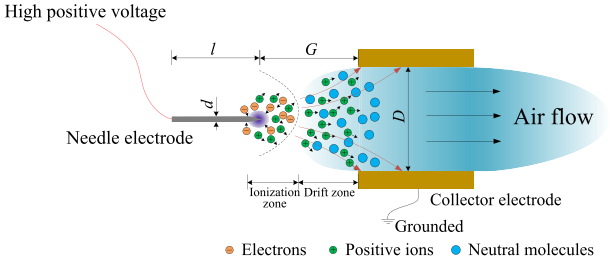

Fig. 1. Physical model and principles of ionic wind formation.

2. Physical model and mathematical formulation

2.1. Physical model

As shown in Fig. 1, the ionic wind generator comprises a ring (collector) electrode with a diameter D and a needle electrode with a diameter d and a length l. The distance between electrodes is defined as G. Air is introduced at the inlet and an impinging flow forms out of the outlet. Based on our previous study on configuration optimization of ionic wind generators with needle-to-ring electrodes, the optimal ratio G/D to obtain the maximum velocity of air flow is 0.2–0.3 [23]. The optimized parameters of the ionic wind generator are shown in Table 1.

A heated square plate made of Cu was added at the outlet of the generator to study the cooling performance of the ionic wind. The physical model is shown in Fig. 2. The length of the square plate (W) is 80 mm and the plate is heated with a heat flux of q. Air is introduced at the inlet, and an impinging flow forms out of the outlet. The plate is then cooled by the impinging flow of the generator.

2.2. Governing equation and boundary conditions

To obtain the electric field, flow, and heat-transfer characteristics of the generator and determine the values of electric potential (V), space-charge density (q), velocity ($\vec{U}$), and temperature (T), the following equations must be solved: Poisson's equation for electrostatics,

$$\nabla^2 V = -\frac{q}{\varepsilon_0} \tag{1}$$

Table 1
Optimized parameters of ionic wind generator.

Parameters	Default value
Needle electrode diameter, d (mm)	0.7
Radius of curvature at the needle tip (μm)	70
Needle electrode length, l (mm)	4
Ring electrode diameter, D (mm)	25
Gap between needle and ring electrodes, G (mm)	5

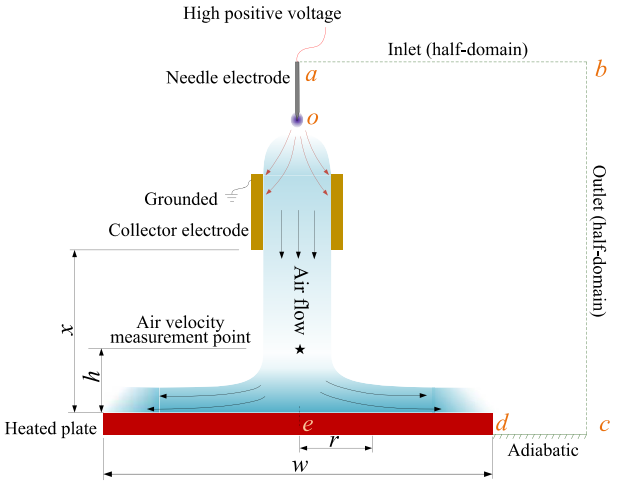

Fig. 2. Physical model (with heated Cu plate).

the current-density-conservation equation,

$$\nabla\vec{J} = 0 \tag{2}$$

the continuum equation,

$$\nabla\cdot(\rho\vec{U}) = 0 \tag{3}$$

and the momentum-conservation equation,

$$\vec{U}\cdot\nabla(\vec{U}) = -\frac{1}{\rho}\nabla p + \nu\nabla^2\vec{U} + \frac{\vec{F_e}}{\rho} \tag{4}$$

Furthermore, the electric field ($\vec{E}$), current density ($\vec{J}$), electric field force ($\vec{F_e}$), and Joule heat (Q_j) can be expressed as follows:

$$\vec{E} = -\nabla V \tag{5}$$

$$\vec{J} = \mu_E\vec{E_q} \tag{6}$$

$$\vec{F_e} = q\vec{E} \tag{7}$$

The boundary conditions of the electrostatic, space-charge, velocity, and heat-transfer fields are provided to solve the preceding equations. For the electrostatic field, the needle electrode is applied with a constant DC voltage and the ring electrode is set to be grounded. It is assumed that no charges are on the other surfaces, including the inlet and outlet. For fluid dynamics, ambient pressures are assigned to the inlet and outlet surfaces, and no-slip boundary conditions are applied to the surfaces of the electrodes and other walls. The detailed boundary conditions are shown in Table 2.

For the charge transport, the intermediate region of the corona and collector electrodes can be divided into ionization and drift zones. The ionization zone of the corona discharge is very thin relative to the transport zone, so the ionization zone can be neglected and it is handled by a boundary condition for charge density on the needle electrode surface. In this simulation, the Kaptzov hypothesis is adopted to obtain the space charge density on the needle electrode surface for different corona discharge voltages. Kaptzov hypothesis states that the electric field at the corona electrode proportionally increases to the applied voltage below the corona onset, but it remains constant as the value at the corona onset voltage after the corona is initiated. This critical electric field on the surface of corona electrode is given by Peek formula. For a needle with a spheroidal tip [24], Peek's value is

$$E_{\text{onset}} = 3.1\times10^6\delta\left(1+\frac{0.308}{\sqrt{0.5\delta r_c}}\right) \tag{8}$$

where r_c is the electrode tip radius of curvature in cm, δ is determine by

$$\delta = \frac{T_0}{T}\frac{P}{P_0}$$

T_0, P_0 are the standard temperature and pressure, respectively. Namely, T_0 is 273.15K, and P_0 is 101325Pa. T and P are the actual temperature and pressure of gas.

Therefore, the initial value of charge density q_0 is assumed and iterated until the electric field strength on the electrode surface is sufficiently close to the value determined by Peek's value. For all of the other boundaries, a zero diffusive charge flux condition is imposed on the surfaces. In order to obtain more accurate results, the ion mobility μ_E in eq. (6) is modified by eq. (9) [24] based on the current-voltage characteristics of the ionic wind generator in the experiment.

$$\mu_E = \frac{Id}{a\varepsilon V(V-V_{\text{onset}})} \tag{9}$$

where I and V are the corona discharge current and voltage, respectively. V_{onset} is the onset corona discharge voltage, and a is a constant value, which is close to 1.58. ε is the gas permittivity, and d is the distance between the two electrodes.

Apart from Eqs. (1)–(7), the energy-conservation equation also must be solved for the heat transfer,

$$\nabla(\vec{U}T) = \nabla\left(\frac{\lambda}{\rho c_p}\nabla T\right) + \frac{Q}{\rho c_p} \tag{10}$$

where Joule heat (Q_e) can be expressed as:

$$Q_e = \vec{J}\cdot\vec{E} = \mu_E q\vec{E}^2 \tag{11}$$

For boundary conditions, the plate is applied with a heat flux of q_f and the inlet and outlet surfaces of the calculation domain are applied with an ambient temperature of T_a = 296.15 K, while the insulation condition is imposed on the outside of the bottom surface of the plate.

2.3. Simulation method

The finite-element method (FEM), as implemented in COMSOL® MultiPhysics software, is conducted to establish the simulation model and solve the coupled equations (1)–(7) and (10). For electrostatics, Poisson's equation is solved in the electrostatic module. For space-charge density, a coefficient partial-differential equation module is conducted to solve the current-density continuity equation. Furthermore, the flow characteristics are simulated in the laminar-flow module. The continuum and momentum conservation equations are solved to obtain the velocity distribution in the computational domain. Fig. 3 shows the computational domain.

3. Experimental apparatus for heated-plate cooling

3.1. Experimental apparatus

The experimental setup of the present study is shown in Fig. 4, and it consists of a high-voltage power supply, a Cu plate with a heating film on the bottom surface, an Agilent signal acquisition system, T-type thermocouples, a laptop, a steady-voltage power supply, and the ionic

Table 2
Boundary conditions.

Surface	Electrostatic field	Space-charge field	Velocity field
Corona electrode (*oa*)[a]	$V = V_0$	$q_c = q_0$	No slip
Collector electrode	$V = 0$	Zero flux	No slip
Inlet (*ab*)	Zero charge	Zero flux	Pressure
Outlet (*bc*)	Zero charge	Zero flux	Pressure
Plate (*de*)	Zero charge	Zero flux	No slip
Others	Zero charge	Zero flux	No slip

[a] Letters in parentheses denote line segments in Fig. 2.

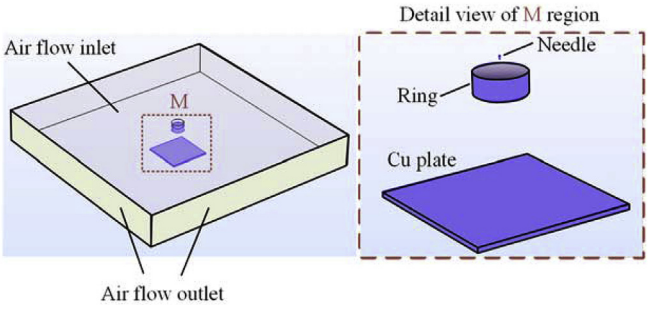

Fig. 3. Computational domain.

wind generator. The material of the needle electrode and ring electrode in the ionic wind generator are wolfram and stainless steel, respectively. The geometric size of the ionic wind generator is consistent with the optimized results shown in Table 1. The steady-voltage power supply is used for powering the heating film. The heating film is of the same size as the Cu plate. Another round heating film representing the hot spot is attached to the center of the above-described heating film. The thermocouples are all fixed in a groove located on the bottom surface of the plate to collect the temperature signals. The bottom side of the heating film is in contact with the thermal insulation material to maintain the adiabatic boundary condition. Table 3 details the name, type, specification, or precision of the instruments used in this experiment. Fig. 5 is a photograph of the experimental device.

3.2. Experimental uncertainty analysis

3.2.1. Velocity uncertainty

The uncertainty of experimental results is usually used to evaluate the magnitude of the error. The velocity errors are mainly induced by the hot-wire anemometer's measurement error and the accidental error in the measurement. The measurement error of the hot-wire anemometer is calculated by:

Table 3
Characteristics of experimental facilities.

Experimental Facilities	Properties
DC high-voltage power supply (Teslaman TRC2020, Dalian Teslaman Technologies Co. Ltd., Dalian, China)	Output voltage range: 0 to +50 kV Resolution: 0.001 kV, 0.001 mA Accuracy: ± 0.1% Stability: less than 0.1% per 8 h after boot-up half an hour later
Agilent signal acquisition system (Agilent 34970A, Agilent Technologies Co. Ltd., Santa Clara, CA, USA)	Temperature measurement range: 100 °C–400 °C[a] Accuracy: ± 1 °C[a] Resolution: 0.001 °C
T-type thermocouples	Temperature measurement range: −100 °C–400 °C Accuracy: ± 0.5 °C
Hot-wire anemometer (Testo 425, Testo SE & Co. KGaA, Schwarzwald, Germany)	Velocity measurement range: 0–20 m/s Accuracy: ± 0.03 m/s +5% of reading Resolution: 0.01 m/s
Steady-voltage power supply (Maisheng MS-303D, Maihao Electronic Technology Co., Ltd., Dongguan, China)	Output voltage range: 0–30 V Accuracy: ± 1% ± 1 dgt[b] Resolution: 0.01 V, 0.01 A

[a] Temperature range and its accuracy are for T-type thermocouples.
[b] dgt denotes resolution.

$$\delta_{vm} = \pm 0.03\text{m/s} + 5\% \text{ of reading} \tag{12}$$

The accidental error δ_{va} is calculated by:

$$\delta_{va} = \pm\sqrt{\frac{\sum_{i=1}^{n}(v_i - \bar{v})^2}{n(n-1)}} \tag{13}$$

where v is the measured mean velocity of 10 s time duration, $\bar{v}$ the mean velocity of five repeated measured values, and n the number of repeated measurements. Therefore, the total uncertainty of the measured velocity is:

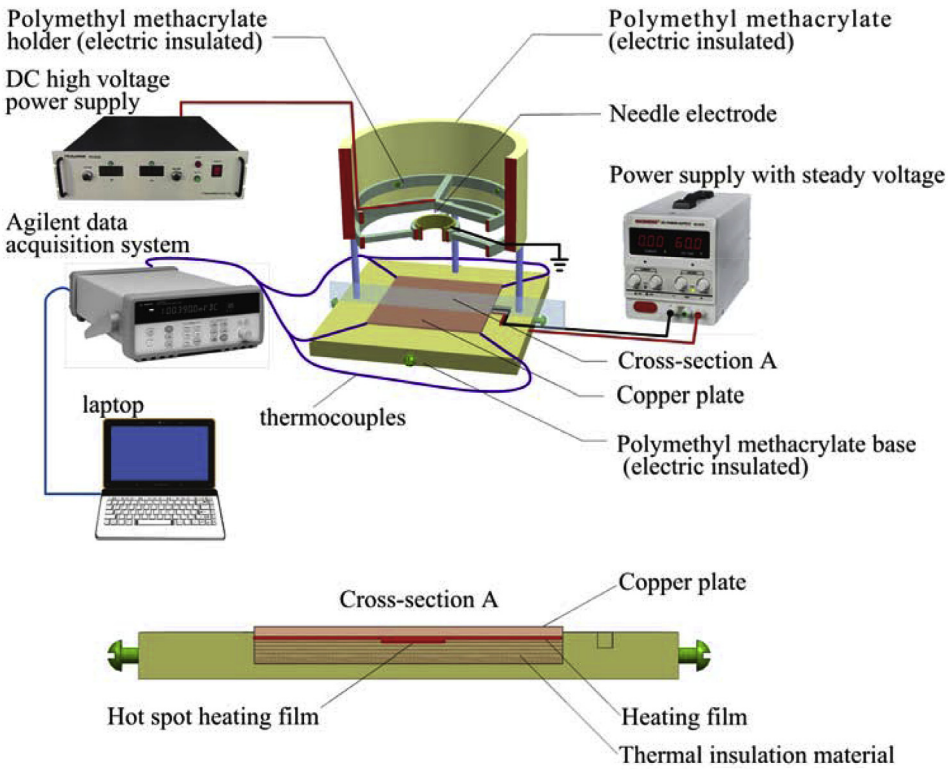

Fig. 4. Experimental setup used for heating plate cooling by ionic wind.

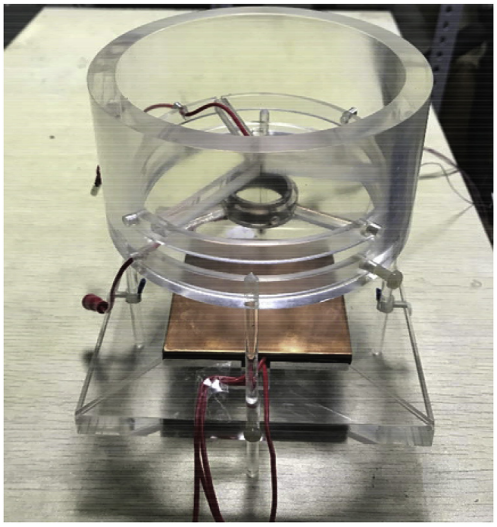

Fig. 5. Photograph of the experimental device used for cooling the heated plate.

$$\delta_{\upsilon} = \pm\sqrt{\delta_{\upsilon m}^2 + \delta_{\upsilon a}^2} \tag{14}$$

Detailed uncertainty values of the airflow velocity are shown in Fig. 6.

3.2.2. Temperature uncertainty

The temperature errors are mainly induced by the thermocouples' measurement errors, display errors of the Agilent data acquisition system, and accidental errors in the measurement. To obtain temperature results of higher accuracy, the thermocouples were calibrated before measurement.

In the temperature calibration, the T-type thermocouples, which were all connected to the Agilent data acquisition system, were placed in a constant temperature tank together with a standard mercurial thermometer (accuracy 0.2 °C, resolution 0.1 °C). After calibration, a linear fitting correlation was obtained for temperature measurement of the thermocouples. Therefore, the uncertainty of the measured results includes three parts: the linear fitting error δ_{tf}, error of the mercurial thermometer δ_{tm}, and measurement accidental error δ_{ta}. For each temperature calibration point, the measured values of thermocouples were taken into the correlation equations, and then the calculated results compared with the readings of the mercurial thermometer to obtain the linear fitting error. The maximum linear fitting error in this calibration is:

$$\delta_{tf,max} = \pm 0.07^{\circ}C \tag{15}$$

the system error of the mercurial thermometer is:

$$\delta_{tm} = \pm .0.\ 2^{\circ}C \tag{16}$$

and the accidental error δ_{ta} is calculated by:

$$\delta_{ta} = \pm\sqrt{\frac{\sum_{i=1}^{n}(T_i - \bar{T})^2}{n(n-1)}} \tag{17}$$

where $\bar{T}$ is the mean temperature of the 10 repeated measured values and n the number of repeated measurements. The maximum accidental error $\delta_{ta,max}$ of all the thermocouples in this experiment is:

$$\delta_{ta,max} = \pm 0.13^{\circ}C \tag{18}$$

Therefore, the maximum total uncertainty of the measured temperature is:

$$\delta_{t} = \pm\sqrt{\delta_{tf,max}^2 + \delta_{tm}^2 + \delta_{ta}^2} \tag{19}$$

After calculation, the maximum absolute error of the measured temperature is:

$$\delta_{t,max} = 0.25^{\circ}C \tag{20}$$

4. Cooling effect of ionic wind generator on heated plate

The ionic wind generator with the optimized configuration was used in the experiment to cool a heated square plate to test the heat-transfer performance. In the following sections, we discuss the current-voltage characteristics, air-flow velocity of the ionic wind generator, and the temperature distribution of the Cu plate.

4.1. Air-flow velocity

Fig. 6 shows the relationship between measured air-flow velocity and applied voltage. The velocity is measured at the point that is 22 mm above the plate surface along the central line of the ionic wind generator, as shown in Fig. 2. The air-flow velocity increases gradually with increasing applied voltage. In the experiment, when the voltage approaches 12 kV, the noise in the process of discharge suddenly increases, and the discharge tends to be unstable, which indicates that the voltage of 12 kV is close to the breakdown voltage. The applied voltage should be less than 12 kV to ensure effective and stable operation of the ionic wind generator.

Different corona voltages from 6 kV to 12 kV were taken to simulate the ionic wind and its cooling effect for the copper plate. Both the numerical and experimental results of velocity at the monitored point are also shown in Fig. 6. The results of the experiment and numerical simulation agree well with each other at low voltages, less than 9 kV, but a deviation exists if the voltage is larger than 9 kV. This is because Peek's formula is only applicable to the corona electrode with a uniform electrode field strength on its surface after the corona is initiated. For the case of a needle electrode, using Peek's formula for simplification will obtain a good result, if the needle is not extremely sharp, radius of curvature at the tip larger than 90 μm [24]. For a sharp needle, the shape of its tip is random and complex from the microscopic view, and may not be approximately a spherical geometry as shown in Fig. 7. This is a major reason for numerical simulation deviation. Besides, the manufacturing roughness, which can affect the electrical field strength on the electrode surface, may be another reason affecting the simulation accuracy.

Since a hot-wire anemometer can only measure the air-flow velocity at a single point, a numerical method is used to obtain the velocity distribution of the entire flow field. Fig. 8 shows the results of velocity distributions at corona voltage 11 kV and electric field lines of the simulation model. The electric field lines represent the direction of electric field force, which is the driving force of the air flow. It can be seen from Fig. 8 that air flow generated by an ionic wind generator with

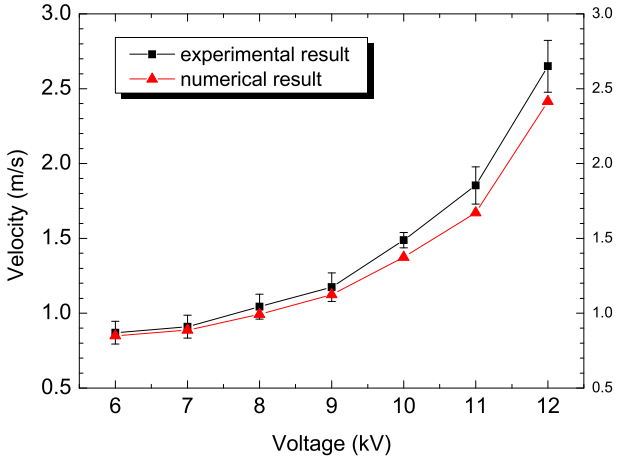

Fig. 6. Air-flow velocity at different applied voltages.

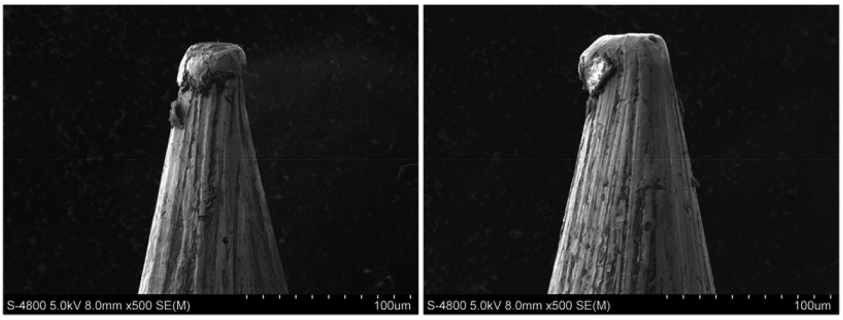

Fig. 7. Shapes of a needle tip shown under a scanning electron microscope.

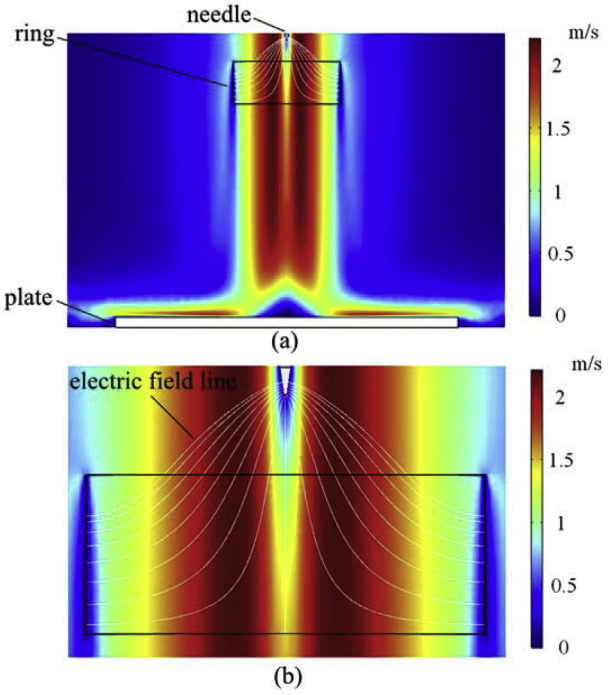

Fig. 8. Air-flow velocity distribution of cooling the plate using ionic wind generator at applied voltage 11 kV: (a) whole view of the velocity distribution; (b) local distribution of the velocity and the electric field lines in the ionic wind generator.

a needle-ring electrode configuration is similar to jet flow. Air flow coming out from the ring outlet directly impinges the surface of the plate, and then spreads along the plate surface, in which process heat is removed from the plate through convection. Air-flow velocity is high in most areas around the axis of the needle electrode (> 1.5 m/s), but it is lower near the surface of the ring electrode. This is because the closer the distance from the point to the surface of the ring is, the greater the angle between the field line and the axis of the ring will be. Near the ring electrode's surface, the electric field line is nearly perpendicular to the central axis of the ring, as shown in Fig. 8 (b). As a result, the axial component of the electric field force (along the needle axis) loading on the air particles gradually decreases, and the macroscopic manifestation is the gradual reduction of air-flow velocity.

4.2. Temperature distribution of plate with uniform heat flux

To show the effects of voltage and heat flux on the temperature distribution of a plate under ionic wind cooling, Fig. 9(a) presents the arrangement of thermocouples on the plate surface. Fig. 9 (b) shows a comparison of the temperature between the numerical and experimental results of temperature distribution along the radial direction of the plate heated by a uniform heat flux of 1 kW/m2 at three different applied voltages, namely, 9 kV, 10 kV and 11 kV, for the ionic wind generator. It can be seen from Fig. 9(b) that the temperature distribution of along the plate surface is relatively uniform, which is attributed to the high thermal diffusivity of copper, and the mean temperature of the plate at applied voltage 11 kV is 53.14 °C. All the results at the above three different corona voltages obtained by the two methods are in good agreement. The maximum deviation is less than 2.8%, which indicates that the numerical method is reliable.

Fig. 10 presents the temperature distributions along the radial direction of the plate surface cooled by ionic wind with different applied voltages and heat fluxes. In Fig. 10, r is the distance between the measurement point and the plate center. It can be seen from the figure that when the plate is heated by a uniform heat flux, the temperature distribution in most areas around the center of the plate is relatively

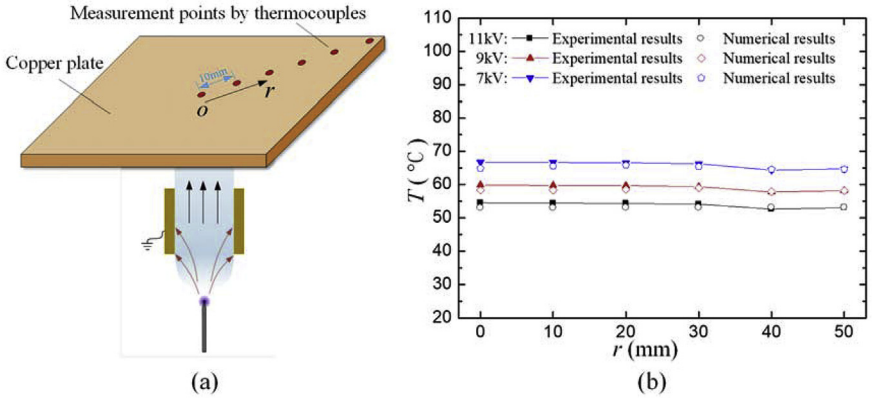

Fig. 9. Temperature distribution of the plate: (a) thermocouples arrangement; (b) comparison of the temperature between the numerical and experimental results along the radial direction of the plate heated by heat flux 1 kW/m^2 at different voltages.

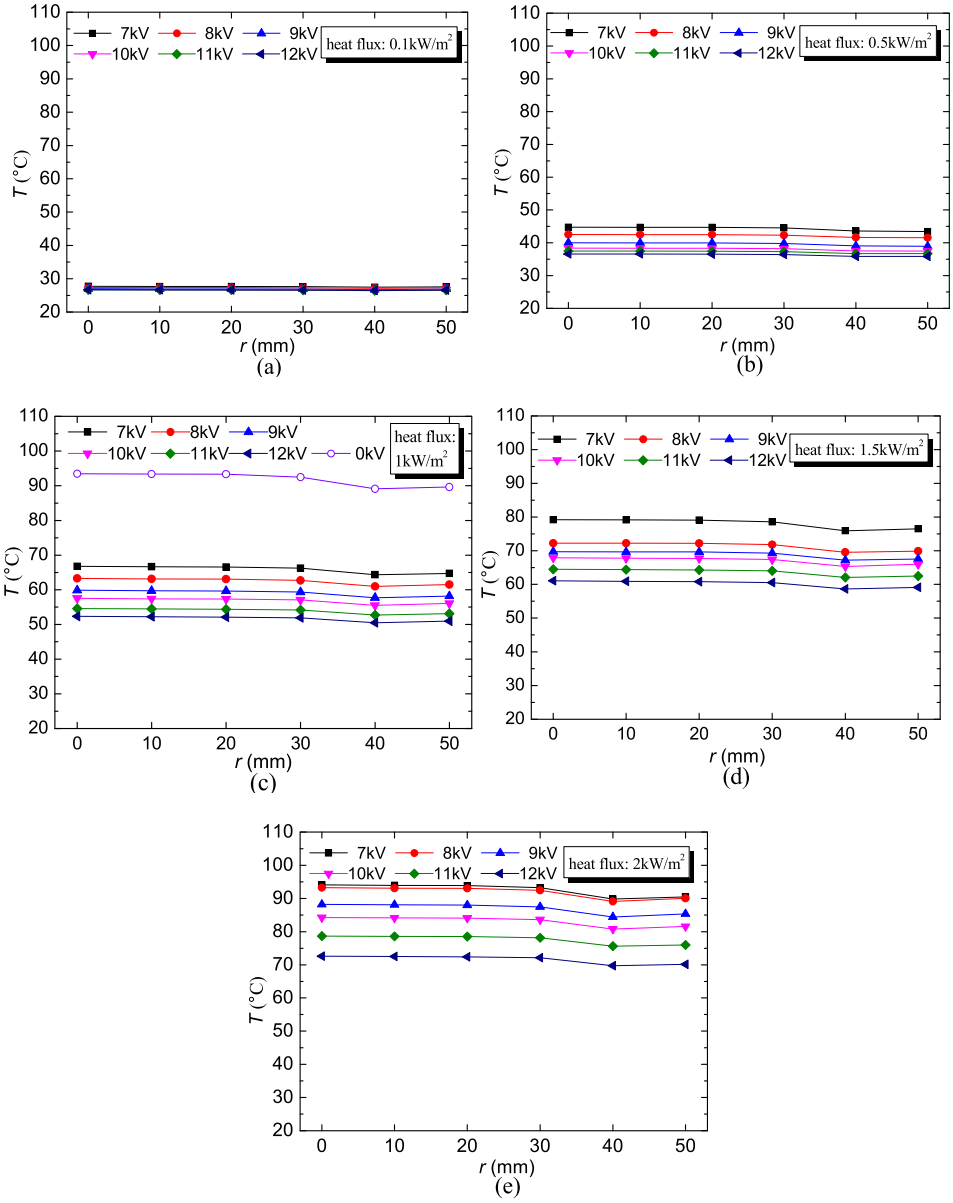

Fig. 10. Temperature distribution along the radial direction of the plate at different. voltagesL: (a) plate heat flux 0.1 kW/m^2; (b) plate heat flux 0.5 kW/m^2; (c) plate heat flux 1 kW/m^2; (d) plate heat flux 1.5 kW/m^2; and (e) plate heat flux 2 kW/m^2.

uniform, and the temperature decreases only in the areas close to the edge of the plate. This is because, although the impingement cooling of ionic wind may lead to a large radial temperature difference, the material of the plate is Cu, which has a high thermal diffusion rate, thus making the temperature of the plate tend to be more uniform. However, considering the thickness of the Cu plate, heat dissipation can occur at the side surface of the plate, resulting in a decrease in the temperature of the edge area of the plate.

When the heating flux is 100 W/m^2, the plate-surface temperature maintains a relatively low value (slightly higher than ambient temperature, 23 °C) because of the low amount of heat flux added to the plate. In addition, the applied voltage in the corona discharge has nearly no effects on the plate temperature distribution, as shown in Fig. 10(a). With increasing heat flux, the temperature of plate gradually increases, and the influence of discharge voltage becomes increasingly more obvious, as shown in Fig. 10 (b)–9(e). With a heat flux of 1 kW/m^2, the plate temperature generally drops by approximately 2 °C upon a discharge-voltage increase of 1 kV. Compared with the plate-surface temperature in the natural convection condition (without the cooling of the ionic wind generator), the plate temperature drops by nearly 30 °C when the ionic wind generator is working, as shown in Fig. 10(c). When the heat flux of the plate increases to 2 kW/m^2, the plate temperature generally drops by approximately 4 °C with an increase of 1 kV in corona discharge voltage. In this situation, the ionic wind device with lower discharge voltage is unable to cool the heated plate effectively, as shown in Fig. 10(e). Moreover, in the case of natural convection, the heating film was found to be damaged when the plate was heated by a heat flux larger than 1 kW/m^2. The heated plate with a uniform heat flux below 2 kW/m^2 could be cooled to lower than 80 °C by the ionic wind generator at an applied voltage of 11 kV.

4.3. Effect of hot spot on plate

The temperature distribution of the plate with a hot spot, as well as the influence of hot-spot heat flux and the size of hot-spot area on temperature distribution, were the next objects studied. The heat flux of the region outside the hot-spot area was kept at a constant value of 1 kW/m^2.

Fig. 11 shows the radial temperature distribution of the plate with four different hot-spot sizes (hot-spot radii of 7.5, 10, 12.5, and 15 mm) and different heat-flux values. The temperatures were measured at a corona discharge voltage of 11 kV. It can be seen from Fig. 10 that, compared with experimental results of natural convection, ionic wind can effectively cool the plate (a temperature drop of at least 45 °C was observed). However, the temperature distribution along the radial direction of the plate is no longer uniform, which is different from the results with uniform heat flux shown in Fig. 10. Upon increasing the heat flux of the hot spot, the non-uniformity of the temperature along the radial direction became more obvious. The reason may be that the hot spot makes the temperature of the central area of the plate higher than that of other areas, and the temperature difference gradually increases with increasing hot-spot heat flux.

As shown in Fig. 11 (a), with a hot-spot radius of 7.5 mm and hot-spot heat flux of 2 kW/m^2, the temperature difference between the center of the plate and the surrounding area is small. With increasing hot-spot heat flux, the temperature in the central region of the plate rises faster, and the temperature difference gradually increases. When the hot-spot heat flux approaches 12 kW/m^2, the temperature difference is close to 2 °C. Similar results were found for other hot-spot radii, as shown in Figs. 11(b)–10(d). When the hot-spot radius was smaller than 15 mm and the hot-spot heat flux lower than 12 kW/m^2, the surface temperature of the plate could be maintained below 80 °C.

By comparing the differences among the sub-figures in Fig. 11, it can be seen that, in addition to the influence of hot-spot heat flux on the plate temperature distribution, the size of the hot spot also affects plate temperature distribution. To study the influence of hot-spot size on plate temperature distribution, Fig. 12 shows the plate temperature distribution with hot spots of different sizes under a discharge voltage of 11 kV and hot-spot heat flux of 12 kW/m^2.

It can be seen from Fig. 12 that if the hot-spot heat flux is kept constant, the overall temperature of the plate increases and the high-temperature area in the center of the plate gradually expands with

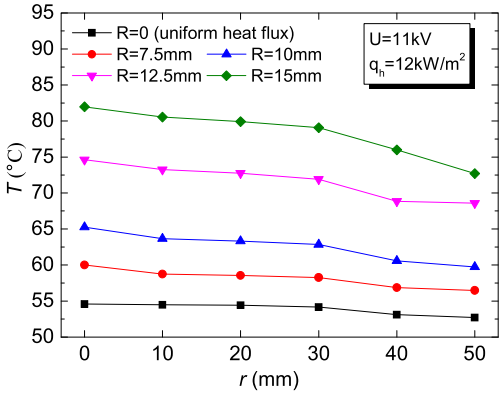

Fig. 12. Temperature distribution along the radial direction of the plate with different hot spot radius at applied voltage 11 kV and plate heat flux 12 kW/m^2

increasing hot-spot radius. For example, in the case in which the hot-spot radius is 7.5 mm, the temperature increases gradually with decreasing radius in the area within 10 mm of the plate center. However, in the region beyond a radius of 10 mm, the temperature distribution is relatively uniform, and the temperature only decreases at the edge of the plate (r > 30 mm). For the case in which the hot-spot radius is 15 mm, the area affected by the hot spot gradually expands, and the radius of affected area reaches 30 mm. There is no region of relatively uniform temperature distribution on the surface of the plate. For the overall temperature of the plate, the surface temperature gradually decreases increasing radius. This is because as the hot-spot area increases, more heat is generated in the center of the plate, and the heat that is generated near the edge of the plate still retains its original temperature value. Finally, the temperature distribution is more uneven.

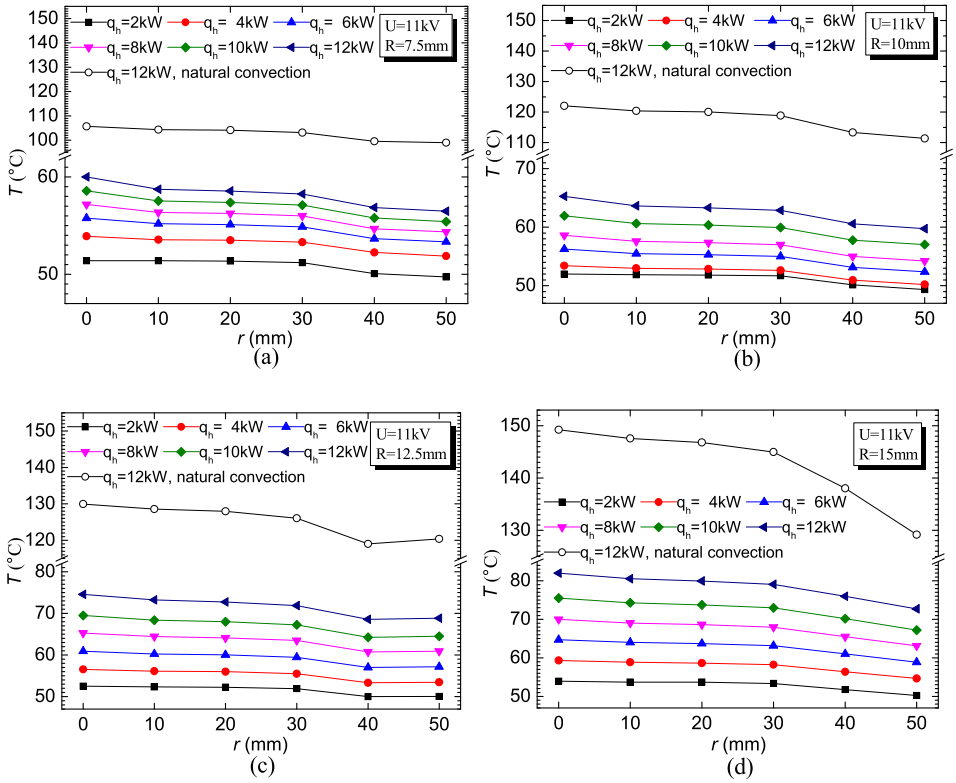

Fig. 11. Temperature distribution along the radial direction of the plate with different hot spot heat flux q_h (in kW/m^2) at applied voltage 11 kV: (a) hot spot radius 7.5 mm; (b) hot spot radius 10 mm; (c) hot spot radius 12.5 mm; and (d) hot spot radius 15 mm.

4.4. Effect of plate thickness on the temperature results

In order to obtain the influence of the thickness of the copper plate on the temperature result, the temperatures of the copper plate were measured with different plate thickness (thickness of 4 mm, 5 mm) heated by a uniform heat flux under ionic wind cooling, which was generated by corona discharge with different voltages, and the final results were compared with the temperature distribution of copper plate with thickness of 2.5 mm, as shown in Fig. 13. It can be seen from the figure that the increase in the copper plate thickness has little influence on the final temperature distribution, and the temperature difference at the same location is not obvious. This is attributed to the high thermal conductivity of the material Cu, which is up to 398W/(m·K). This is also verified by the numerical results, as shown in Fig. 13 (c), which shows the temperature distribution along the vertical cross-section of the Cu plate with different thickness. The results indicates that the temperature distribution along the plate thickness is approximately uniform and does not change significantly with the plate thickness. However, the increase in thickness does lead to a slight increase in the thermal resistance of the copper plate, which is the source of these minor differences. Therefore, the plate with the maximum thickness is always slightly higher in temperature.

Fig. 14 shows the influence of plate thickness on the hot spot effect. The hot spot heat flux are 4 kW/m^2, 8 kW/m^2 and 12 kW/m^2, respectively. To take the hot spot size into account, two different hot spot radii of 7.5 mm and 12.5 mm are investigated here. The discharge voltage of ionic wind is consistent with the voltage cooling for 2.5 mm copper plate heated by a hot spot heat flux in this manuscript, namely 11 kV. It can be seen from Fig. 14 that the change of thickness also has a slight impact on the temperature value of copper plate surface, but such difference is not obvious. Comparing the two panels in Fig. 14, the temperature distribution on the copper plate surface becomes more uneven with the increasing hot spot radius, and the temperature difference at a certain heat flux difference also increases with increasing hot spot radius.

5. Conclusions

In this study, a three-dimensional numerical simulation and experimental study was conducted to examine the cooling effect of an ionic wind generator with a needle-to-ring electrode. The temperature distributions of a Cu plate heated by heat flux with uniform distribution and by heat flux with a local hot spot under the cooling effect of the ionic wind generator were analyzed. The following conclusions were drawn.

1. Air-flow velocity is high in most areas around the axis of the needle electrode (> 1.5 m/s), but it is lower near the surface of the ring electrode, as a result of the decrease of the axial component of the electric field force. The applied voltage should be less than the threshold voltage of spark discharge to ensure effective and stable operation of the ionic wind generator. If not, breakdown will occur.
2. When the plate is heated by a uniform heat flux, the temperature distribution around the central plate is relatively uniform, and the temperature decreases only in the areas close to the edge of the plate. With increasing heat flux of the plate, the overall temperature of the plate gradually increases, and the influence of discharge voltage on temperature distribution becomes increasingly more obvious.
3. When the plate is heated by a heat flux with a hot spot, the temperature distribution along the radial direction of the plate is more non-uniform than without the hot spot, and the higher the hot-spot heat flux, the more obvious the non-uniformity of the temperature will be.
4. If the hot-spot heat flux is kept constant, the overall temperature of the plate will increase and the high-temperature area in the center of

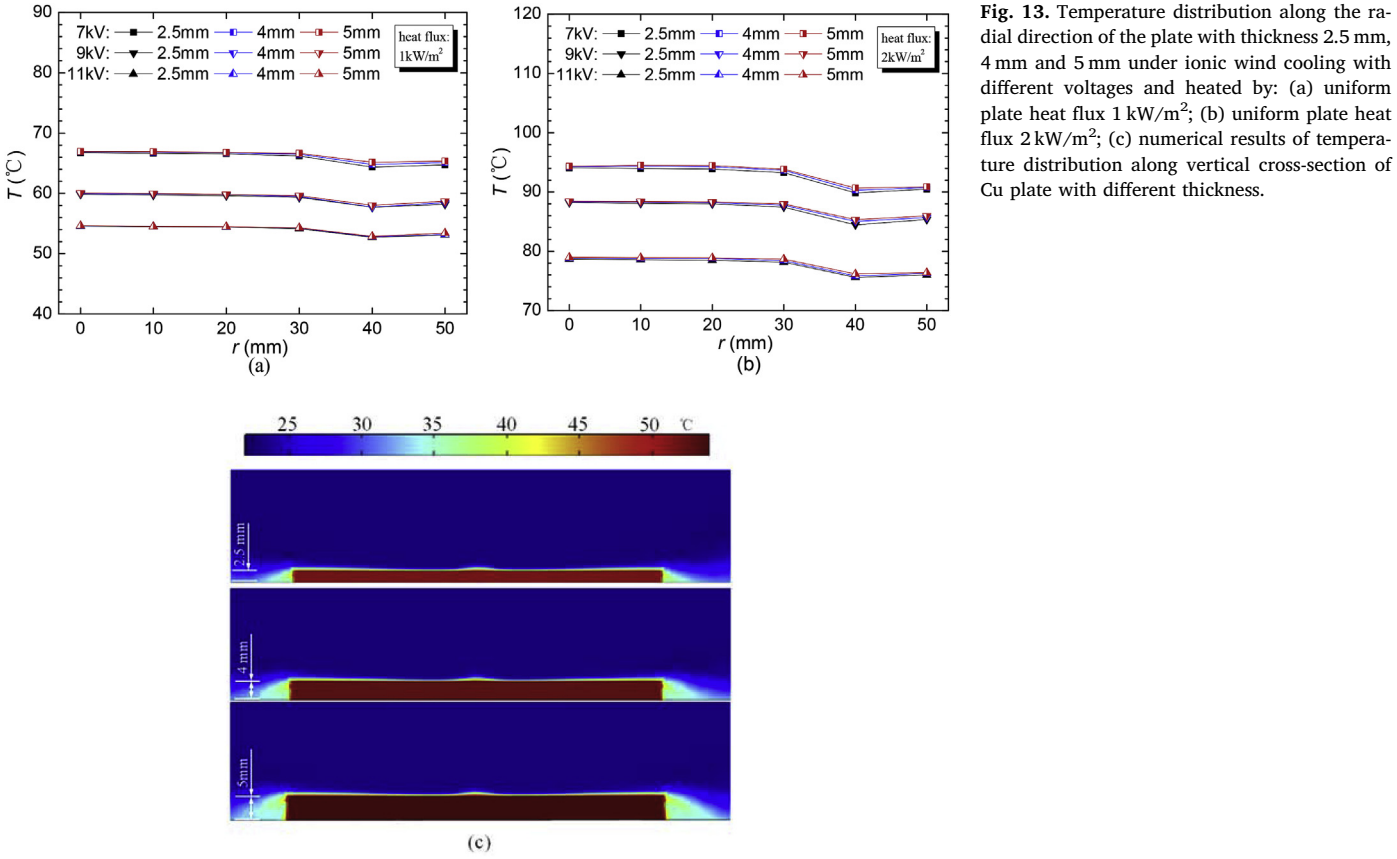

Fig. 13. Temperature distribution along the radial direction of the plate with thickness 2.5 mm, 4 mm and 5 mm under ionic wind cooling with different voltages and heated by: (a) uniform plate heat flux 1 kW/m^2; (b) uniform plate heat flux 2 kW/m^2; (c) numerical results of temperature distribution along vertical cross-section of Cu plate with different thickness.

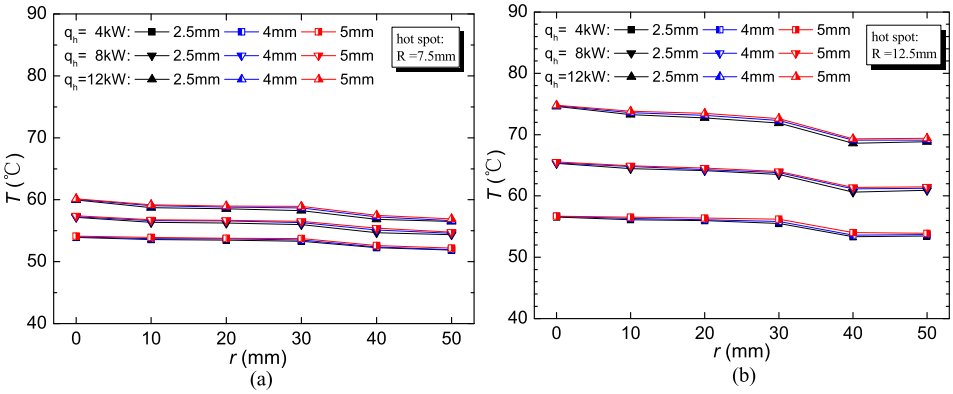

Fig. 14. Temperature distribution along the radial direction of the plate with thickness 2.5 mm, 4 mm and 5 mm heated by different hot spot heat flux q_h (in kW/m^2) at applied voltage 11 kV: (a) hot spot radius 7.5 mm; (b) hot spot radius 12.5 mm.

the plate will gradually expand with increasing hot-spot radius. Besides, the increase in the copper plate thickness has little influence on the final temperature distribution.

5. The heated plate with a uniform heat flux below 2 kW/m^2 could be cooled to lower than 80 °C by the ionic wind generator at an applied voltage of 11 kV. When the plate is heated by a non-uniform heat flux with a hot spot, compared with the experimental results of natural convection, ionic wind can effectively reduce the temperature of the plate (a temperature drop of at least 45 °C was observed).

Acknowledgment

This work is supported by the National Natural Science Foundation of China (No. 51576155) and the Foundation for Innovative Research Groups of the National Natural Science Foundation of China (No.51721004).

References

[1] N.E. Jewell-Larsen, H. Ran, Y. Zhang, M.K. Schwiebert, K.A. Honer, Electrohydrodynamic (EHD) cooled laptop, Semiconductor Thermal Measurement and Management Symposium, 25th Annual IEEE, 2009, pp. 261–266.
[2] C. Jen-Shih, H. Tsubone, G.D. Harvel, K. Urashima, Narrow-flow-channel-driven EHD gas pump for an advanced thermal management of microelectronics, IEEE Trans. Ind. Appl. 46 (2010) 1151–1158.
[3] B.A. Kozlov, V.I. Solovyov, Electric wind in electrode systems with corona points, Tech. Phys. 52 (2007) 892–897.
[4] E. Karakas, A. Begum, M. Laroussi, A positive corona-based ion wind generator, IEEE Trans. Plasma Sci. 36 (2008) 950–951.
[5] V. Boucinha, P. Magnier, R. Weber, A. Leroy-Chesneau, B. Dong, D. Hong, R. Joussot, Characterization of the ionic wind induced by a sine DBD actuator used for laminar-to-turbulent transition delay, 4th Flow Control Conference, 2008, p. 4210.
[6] E. Moreau, Airflow control by non-thermal plasma actuators, J. Phys. D Appl. Phys. 40 (2007) 605–636.
[7] H. Ait Said, H. Nouri, Y. Zebboudj, Effect of air flow on corona discharge in wire-to-plate electrostatic precipitator, J. Electrost. 73 (2015) 19–25.
[8] K.N. Kiousis, A.X. Moronis, W.G. Früh, Computational Problems in Engineering, Springer, Cham, 2014.
[9] L. Zhao, K. Adamiak, EHD flow in air produced by electric corona discharge in pin–plate configuration, J. Electrost. 63 (2005) 337–350.
[10] A. Ongkodjojo Ong, A.R. Abramson, N.C. Tien, Electrohydrodynamic micro-fabricated ionic wind pumps for thermal management applications, J. Heat Tran. 136 (2014).
[11] B.L. Owsenek, J. Seyedyagoobi, R.H. Page, Experimental investigation of corona wind heat-transfer enhancement with a heated horizontal flat-plate, J Heat Trans-T Asme 117 (1995) 309–315.
[12] D.B. Go, S.V. Garimella, T.S. Fisher, Ionic winds for locally enhanced cooling, J. Appl. Phys. 102 (2007) 1–8.
[13] R.T. Huang, W.J. Sheu, C.C. Wang, Heat transfer enhancement by needle-arrayed electrodes - an EHD integrated cooling system, Energy Convers. Manag. 50 (2009) 1789–1796.
[14] M. Shakouri Pour, E. Esmaeilzadeh, Experimental investigation of convective heat transfer enhancement from 3D-shape heat sources by EHD actuator in duct flow, Exp. Therm. Fluid Sci. 35 (2011) 1383–1391.
[15] L. Dascalescu, A. Samuila, D. Rafiroiu, A. Iuga, R. Morar, Multiple-needle corona electrodes for electrostatic processes application, IEEE Trans. Ind. Appl. 35 (1999) 543–548.
[16] J.-D. Moon, D.-h. Hwang, An EHD gas pump utilizing a ring needle electrode, IEEE Trans. Dielectr. Electr. Insul. 16 (2009) 352–358.
[17] M. Rickard, D. Dunn-Rankin, Numerical simulation of a tubular ion-driven wind generator, J. Electrost. 65 (2007) 646–654.
[18] E. Moreau, G. Touchard, Enhancing the mechanical efficiency of electric wind in corona discharges, J. Electrost. 66 (2008) 39–44.
[19] H. Kawamoto, S. Umezu, Electrostatic micro-ozone fan that utilizes ionic wind induced in pin-to-plate corona discharge system, J. Electrost. 66 (2008) 445–454.
[20] W. Qiu, L. Xia, X. Tan, L. Yang, The velocity characteristics of a serial-staged EHD gas pump in air, IEEE Trans. Plasma Sci. 38 (2010) 2848–2853.
[21] S.J. Lee, L. Li, K. Kwon, W. Kim, D. Kim, Parallel integration of ionic wind generators on PCBs for enhancing flow rate, Microsyst. Technol. 21 (2015) 1465–1471.
[22] L. Li, S.J. Lee, W. Kim, D. Kim, An empirical model for ionic wind generation by a needle-to-cylinder dc corona discharge, J. Electrost. 73 (2015) 125–130.
[23] S. Wang, J. Zhang, W. Tao, Numerical parametric study on the performance and optimal configuration of ionic wind generators with needle-to-ring electrode, 4th International Workshop on Heat Transfer, 2017.
[24] K. Adamiak, P. Atten, Simulation of corona discharge in point–plane configuration, J. Electrost. 61 (2004) 85–98.